PDE-based reconstruction of the cerebral cortex from MR images

Sergey Osechinskiy and Frithjof Kruggel

Abstract— The topologically correct and geometrically accurate reconstruction of the cerebral cortex from magnetic resonance (MR) images is an important step in quantitative analysis of the human brain structure, *e.g.* in cortical thickness measurement studies. Limited resolution of MR images, noise, intensity inhomogeneities, and partial volume effects can all contribute to geometrical inaccuracies and topological errors in the model of cortical surfaces. For example, unresolved touching banks of gray matter (GM) in narrow sulci pose a particular challenge for an automated algorithm, requiring specific steps for the recovery of separating boundaries. We present a method for the automated reconstruction of the cortical compartment from MR images. The method is based on several partial differential equation (PDE) modelling stages. First, a potential field is computed in an electrostatic model with GM posing as an insulating dielectric layer surrounding a charged conductive white matter (WM) object. Second, geodesic distances from WM along the streamlines of the potential field are computed in a Eulerian framework PDE. Third, a digital skeleton surface separating GM sulcal banks is derived by finding shocks in the distance field. At the last stage, a geometric deformable model based on the level set PDE is used to reconstruct the outer cortical surface by advection along the gradient of the distance or potential field. The rule preserving the digital topology, and the skeleton of the distance field resolving fused adjacent banks in sulci, constrain the deformable model evolution. In addition, the deformable model may use the distance field as a constraint on thickness of the reconstructed cortical layer.

I. INTRODUCTION

Digital reconstruction of the cerebral cortex from magnetic resonance (MR) images is an important step in quantitative analysis of the human brain structure, *e.g.* in analysis of cortical folding patterns, in brain morphometry, and particularly in cortical thickness measurement studies. Cortical reconstruction, *i.e.* the derivation of a computerized representation of the cortical layer based on three-dimensional (3D) images of the brain, must be geometrically accurate and topologically correct in order to provide valid and accurate quantitative measures of brain structure. The cerebral cortex is a thin layer of neural tissue, called gray matter (GM), on the outer side of the white matter (WM). The cortex has a 3D geometry of a highly-folded layer with spatially varying curvature and thickness (1-5 mm, average thickness around 2.5 mm [1]). In theory, the cortical layer can be represented as the inner space between two cortical surfaces, each surface being topologically homeomorphic to a 3D sphere. In practice, limited spatial resolution of MR images, noise, intensity inhomogeneities, and partial volume effects can all be the sources of geometrical inaccuracies and topological

errors in the reconstructed cortical model. In particular, the opposite banks of gray matter in deep sulci are not always resolved as separate, and can appear fused together, leading to invalid models of the cortical layer and propagating errors further into quantitative measurements, e.g. of cortical thickness. This may present a particular challenge for an automated reconstruction algorithm, requiring specific means for an automatic detection and correction of topologically and geometrically problematic cases.

Reconstruction of cortical surface models received considerable attention in biomedical image analysis research. Fischl *et al.* in [2] provide an overview of topology-enforcing and topology-correcting methods for the construction of cortical models, and present a surface mesh based algorithm for finding and correcting the topological defects. Kim *et al.* in [3] present a deformable mesh algorithm, called constrained Laplacian anatomic segmentation using proximity (CLASP). The algorithm computes a Laplacian field mapping between the GM/WM interface and the skeleton of the partial volume classification of the cerebrospinal fluid (CSF). The Laplacian map is then integrated into the the deformable model's objective function, driving mesh vertices into locations with higher values of the Laplacian field, and simultaneously serving as a constraint on the distance from the GM/WM initial surface. The method in [3] depends on accurate extraction of the CSF skeleton, which may be compromised at locations, where the fused GM sulcal banks are not resolved even by partial volume CSF voxels. Zeng *et al.* in [4] provide a different approach to the distance-constrained reconstruction of the inner and outer cortical surface, using the distance-coupled evolution of two implicit surfaces in the level set framework. However, this approach does not constrain topological changes in the evolving coupled surfaces, and in some cases, the distance coupling may be too strong, resulting in geometrical inaccuracies. Han *et al.* [1] describe a method for automatic reconstruction of cortical surfaces, called CRUISE, which is built around a deformable model using the level set method. To help resolve the cortical banks in sulci, a thin digital separating barrier is constructed using the Anatomically Consistent Enhancement (ACE) algorithm [1], [5], which finds a skeleton of the weighted distance function computed from the Eikonal equation with a speed function modulated by the CSF class membership. At the core of the CRUISE method is a topology-preserving geometric deformable surface model (TGDM) [1], [5], [6], which models evolution of a level set function under the influence of signed pressure forces computed from tissue class membership values, and curvature forces defined by the surface geometry. Optionally [1], the TGDM can include

S. Osechinskiy and F. Kruggel are with the Department of Biomedical Engineering, University of California, Irvine CA 92697, USA {sosechin,fkruggel}@uci.edu

the advection forces determined by a gradient vector flow (GVF) derived from an image intensity edge map, which is often used in snake models (see [7]).

We found that available software is not suitable for dealing with the analysis of MR imaging data at a much higher resolution and a different image contrast than standard images. We present a method for the automatic reconstruction of the cortical compartment from MR images, which is based on several partial differential equation (PDE) modelling stages. Our method is inspired by the work of Han *et al.* [1], but introduces a different perspective, consolidating all algorithmic stages around the key model of the potential field. The method proceeds as follows: First, a potential field is computed using an electrostatic model, where WM poses as a charged conductive object, and GM poses as a dielectric insulating layer with permittivity proportional to GM class probability values. Second, distances from WM along the streamlines of the potential field are found in Eulerian framework as a solution of a PDE, without explicitly constructing the streamline trajectories. Third, a binary skeleton separating GM banks is derived by finding shocks in the distance field, similarly to skeletonization in the ACE algorithm in [1]. At the last stage, a geometric deformable model based on the level set PDE is used to reconstruct the outer cortical surface by advection along the gradient of the potential or distance field computed at earlier stages. The evolution of the deformable model is constrained topologically by a simple-point based rule preserving the digital topology (similarly to the TGDM in [1]), and by the skeleton of the distance field, which helps to resolve the touching GM banks. In addition, the distance field itself may be used as an optional constraint on the thickness of the reconstructed cortical layer.

II. METHODS

The method is described in 3D, but can be applied to 2D images as well. Let $\vec{r} = (x, y, z)$ denote a point in the discretized 3D space $\mathbb{R}^3$, $\Omega \subset \mathbb{R}^3$ denote the image domain, and $\Gamma(\Omega)$ denote the domain boundary. The input to our algorithm consists of the following data derived from a raw MR image: 1) WM and GM tissue class probability images, $P_w(\vec{r})$ and $P_g(\vec{r})$; 2) a refined segmentation of WM, $B_w(\vec{r})$; ($\vec{r} \in \Omega$). The refined WM segmentation can be supplied in the form of a binary image, an edited class membership, or a level set function. Let $\Omega_w \subset \Omega$ denote the binary domain of the WM object ($B_w(\vec{r}) = 1 \iff \vec{r} \in \Omega_w$). Image preprocessing, tissue classification, and WM segmentation/editing steps have been described elsewhere (*e.g.* see [1], [8] for details).

A. Electric field model

A potential field is found as a solution to the PDE modelling an electric field around a charged conductive WM object insulated by a dielectric GM layer having spatially inhomogeneous electric permittivity proportional to $P_g(\vec{r})$. In such a model, it is qualitatively expected that the flux of the electric field will be confined in regions of higher permittivity, *i.e.* where GM class probability is higher, therefore trajectories following the streamlines of the electric field will trace through the GM layer before exiting into the background space. Let $\varphi(\vec{r})$ denote a potential field, a scalar function defined over Ω. The gradient of the potential $\vec{E}(\vec{r}) = \nabla\varphi$ is a conservative vector field, which is irrotational ($\nabla \times \vec{E} = 0$). Let $\varepsilon(\vec{r})$ denote another scalar function, which will be called permittivity. Permittivity can be computed from class probabilities as follows:

$$\varepsilon(\vec{r}) = 1 + (\varepsilon_{\max} - 1)(P_w(\vec{r}) + P_g(\vec{r})), \tag{1}$$

where $\varepsilon_{\max}$ is the maximum permittivity of the insulating layer. Thus permittivity is close to $\varepsilon_{\max}$ when WM and/or GM class probabilities are high, and is close to 1 when they are low. The potential field is found as a solution of Maxwell's equation for an electric field inside inhomogeneous dielectric medium in the absence of free charges:

$$\nabla(\varepsilon(\vec{r})\vec{E}(\vec{r})) = \nabla\varepsilon\nabla\varphi + \varepsilon\Delta\varphi = 0. \tag{2}$$

The above equation (2) assumes that the dielectric medium has linear and isotropic properties, therefore ε is a scalar, not a tensor. Boundary conditions are specified as $\varphi(\vec{r} \in \Omega_w) = V_{\max}$ and $\varphi(\vec{r} \in \Gamma(\Omega)) = 0$, where $V_{\max}$ is the potential of the WM object. The solution of the PDE $\varphi(\vec{r} \in \Omega \setminus \Omega_w)$ can be obtained as a steady state solution ($\frac{\partial\varphi}{\partial t} \to 0$) of a nonstationary equation:

$$\frac{\partial\varphi}{\partial t} = \nabla\varepsilon\nabla\varphi + \varepsilon\Delta\varphi. \tag{3}$$

The equation (3) can also be viewed as describing the diffusion in inhomogeneous medium, where $\varepsilon(\vec{r})$ is a spatially varying but stationary diffusion coefficient, and $\varphi(\vec{r}, t)$ is the concentration of the diffusing substance. This allows for a different physical interpretation of the model: we seek a steady state spatial distribution of "particles" diffusing from WM source into the medium without sinks and with diffusivity proportional to GM class probability. Qualitatively, it is expected that "particles" would diffuse more freely in GM, therefore the streamlines of the $\nabla\varphi$ field would tend to concentrate in the GM compartment. The equation (3) can be discretized and solved iteratively as described in [9], *e.g.* using the Jacobi method [10].

B. Streamline distance field

Streamlines of the potential field φ are defined as a family of curves that are at each point tangent to the gradient $\nabla\varphi$. Let $d(\vec{s}, \vec{r})$ denote the length of a streamline segment originating at some point in WM boundary $\vec{s} \in \Gamma(\Omega_w)$ and ending in point $\vec{r} \in \Omega \setminus \Omega_w$. If for any point $\vec{r}$ there is one and only one streamline passing through it, then $d(\vec{r})$ defines a distance field. While such one-to-one correspondence always holds for an incompressible flow defined by a Laplacian field ϕ ($\Delta\phi = 0$), it does not hold for compressible flows in general. Fortunately, in our case of the potential flow in linear, isotropic, inhomogeneous medium without sinks and impenetrable barriers, it can be shown that the distance field can be defined. It is possible to compute the distance

field without explicitly finding the streamline curves and integrating trajectories in a Lagrangian framework. Using the method described in [11], the distance field can be found as a solution of a PDE in an Eulerian framework on a fixed grid. We note that $\nabla \varphi / \|\nabla \varphi\|$ is the unit tangent field of the potential field φ. Then it can be shown that the distance field d must satisfy the following PDE:

$$\frac{\nabla \varphi}{\|\nabla \varphi\|} \cdot \nabla d(\vec{r}) = 1, \qquad (4)$$

with the boundary condition $d(\vec{r} \in \Gamma(\Omega_w)) = 0$. The PDE (4) can be solved using the numerical implementation described in [11]. In principle, finite spatial discretization may violate the bijective property of the flow by clamping several streamline paths into one grid point, so the solution $d(\vec{r})$ may experience numerical convergence problems in some grid locations. In practice, we found that such problematic points are very sparse, and do not impede numerical convergence in the computational domain at large. These points are usually detected among other "shocks" in the distance field by a skeletonization method, which is described next.

C. Skeleton of the distance field

Shocks, or singularities of a distance field d are defined as a set of points, where spatial derivatives of the field are not well-behaved, *i.e.* the gradient ∇d is not well defined. Such shocks appear as discontinuities or sinks in the field. Note that even though the potential field in our model should be, in theory, free from the sinks, they may appear in the distance field due to numerical discretization. Let $S \subset \Omega \backslash \Omega_w$, called a skeleton of the distance field, denote a set of grid points, where shocks are detected by a numerical procedure. Such numerical procedure can be based on finite difference approximations to ∇d, as described in the ACE method in [1]. The observation is that a centered finite difference numerical scheme will produce values of $\|\nabla d\|$ that are significantly lower than 1 on the shock points, and are close to unity elsewhere. Then the skeleton can be detected as $S = \{\vec{r} \mid (\vec{r} \in \Omega \backslash \Omega_w) \wedge (d(\vec{r}) > d_{\min}) \wedge (\|\nabla d(\vec{r})\| < T)\}$, where $d_{\min}$ is a minimum distance parameter, and T is a specified threshold value ($T < 1$). Alternatively, the distance field skeleton can be detected with the Hamilton-Jacobi skeleton algorithm [12], [13], which is based on the idea that the flux of the vector field ∇d should be close to zero for points away from shocks, and has large negative/positive values at sink/source shock points, respectively. The algorithm allows efficient numerical implementation [12], where for each grid point $\vec{r}$ the flux of ∇d is computed as a sum of $\vec{n}_{ri} \cdot \nabla d$ over all neighbouring grid points $\vec{r}_i$, where $\vec{n}_{ri}$ denotes an outward normal vector at $\vec{r}_i$ to a unit sphere centered at $\vec{r}$. Since derivatives are not well-behaved in locations close to shocks, numerical approximations of ∇d must be computed using Hamilton-Jacobi essentially nonoscillatory (ENO) or weighted ENO (WENO) interpolants (see [12], [14] for details). As illustrated in Fig. 4, a skeleton of the distance field can be used to guide the cortical reconstruction

algorithm in places where the boundary between cortical banks is otherwise not clearly detectable.

D. Geometric deformable model

The geometric deformable model uses an implicit representation of a surface, embedding it into a so-called level set function, which is a real valued function defined, in our case, on the 3D domain Ω. Let $\phi(\vec{r}, t)$, $\vec{r} \in \Omega$ denote a level set function. Then the evolving interface embedded in the zero level set is $D(t) = \{\vec{r} \in \Omega \mid \phi(\vec{r}, t) = 0\}$ (see [14]). In our model, evolution of the level set function is described by the following PDE:

$$\frac{\partial \phi(\vec{r}, t)}{\partial t} + \vec{V}(\vec{r}) \cdot \nabla \phi(\vec{r}, t) = w_\kappa \kappa(\phi) \|\nabla \phi(\vec{r}, t)\|, \qquad (5)$$

where $\vec{V}$ is the advection velocity vector field, κ is the mean curvature, and w_κ is the weight of the curvature term ($w_\kappa > 0$). The mean curvature of the interface embedded in the level set function is [14]:

$$\kappa = \nabla \cdot \left(\frac{\nabla \phi}{\|\nabla \phi\|} \right). \qquad (6)$$

The advection velocity vector field $\vec{V}(\vec{r})$ is derived from the gradient of the potential field φ (see sect. II-A) or the distance field d (see sect. II-B):

$$\vec{V}(\vec{r}) = \begin{cases} -\beta(\vec{r}) \left(\frac{\nabla \varphi(\vec{r})}{\|\nabla \varphi\|} \right) \\ or \\ \beta(\vec{r}) \left(\frac{\nabla d(\vec{r})}{\|\nabla d\|} \right) \end{cases}, \qquad (7)$$

where $\beta(\vec{r})$ is a stopping/direction-reversal factor computed from the GM/WM class probabilities. For example, the stopping/reversal factor can have a form of a logistic function:

$$\beta(\vec{r}) = \frac{2}{1 + \exp(-K[P_{gw}(\vec{r}) - P_0])} - 1, \qquad (8)$$

where K is the constant controlling the steepness of the slope of the sigmoid curve, and P_0 is the GM class probability threshold value determining the capture range of the deformable model. For spatial regularization, the combined GM and WM class probability $P_{gw}(\vec{r})$ can be calculated as a weighted sum over the 18- or 26-connected neighbourhood N_n of the point $\vec{r}$:

$$P_{gw}(\vec{r}) = \sum_{\vec{r}_i \in \{\vec{r}, N_n(\vec{r})\}, \vec{r}_i \notin S} w_i (P_g(\vec{r}_i) + P_w(\vec{r}_i)), \qquad (9)$$

where w_i are the neighbourhood weights, and the binary skeleton of the distance field S is used for masking of the class probability values in the separating barriers. As an option, the stopping factor β in Eq. (7) can be modified to include the distance-constraining factor:

$$\beta_1 = |\beta(\vec{r})||\gamma(\vec{r})|sgn(\beta, \gamma), \qquad (10)$$

where the sign function is an "OR" combination of two signs:

$$sgn(a, b) = \begin{cases} -1 & \text{if } a < 0 \text{ or } b < 0 \\ 1 & \text{otherwise} \end{cases}, \qquad (11)$$

and the distance-constraining factor γ can also have a form of a logistic function:

$$\gamma(\vec{r}) = \frac{2}{1 + \exp\left(-K\left[\frac{1}{2} - \frac{\min(d(\vec{r}), 2d_{\max})}{2d_{\max}}\right]\right)} - 1. \quad (12)$$

In the equation (12), $d_{\max}$ is a parameter constraining the maximum distance of advection along the streamlines of the gradient field.

Our numerical implementation for solving the level set Eq. (5) is based on the narrow-band algorithm [6], [14], [15]. The initial level set function is computed as a signed-distance function (SDF) of the initial interface, supplied in the refined WM image B_w, using the fast marching method (FMM) [14], [16]. By standard convention, the "inside" points are represented by negative values of the SDF. During the evolution, the level set function $\phi(\vec{r}, t)$ is maintained close to the SDF by periodic reinitialization with the FMM. The advection term in Eq. (5) is discretized based on the upwind differencing scheme (see [14] for details), and the curvature term is discretized along the lines of Eq. (6) using the central differencing scheme [10]. A pseudo-code outlining the narrow-band algorithm is described elsewhere (*e.g.* in [6], [15]). In the Algorithm 1 below, we focus on the algorithmic core part, which deals with the update of the level set function. The update algorithm uses the skeleton of the distance field (sect. II-C) to create barriers for the evolving interface. In addition, the algorithm has a built-in rule preserving the digital topology of the deformed model, similarly to the TGDM in [1], [6]. The topology preserving rule is based on the concept of simple point [17]. By definition, the removal of a simple point does not change the topology of a binary image. Bertrand in [17] provides the algorithm for boolean characterization of 3D simple points based on checking of five basic configurations in the local neighbourhood of a point. Since the digital topology of a binary image depends on the chosen connectivity model, the connectivity must be explicitly stated in the simple point characterization. Let $B(\vec{r}, \phi) = \begin{cases} 1 & \text{if } \phi(\vec{r}, t) \leq 0 \\ 0 & \text{otherwise} \end{cases}$, denote the foreground binary object, and $\overline{B}$ denote its complement, or the background binary object. As in [17], foreground/background objects use the 26-/6-neighbourhood connectivity, respectively. Let $\hat{\phi}$ denote the level set function that has been updated to the value ϕ_{new} at the point $\vec{r}_i$. Then the *IsSimplePoint*$(\phi(\vec{r}, t_k), \phi_{new}, \vec{r}_i)$ function returns *true* if $\vec{r}_i$ is a foreground point ($\phi_{new} \leq 0$) and is a 26-connected simple point in $B(\hat{\phi})$, or is a background point ($\phi_{new} > 0$) and is 6-connected simple point in $\overline{B}(\hat{\phi})$, and otherwise returns *false*.

III. EXPERIMENTAL RESULTS

Our algorithm is implemented in C++ in the Linux environment. The algorithm was evaluated on simulated test cases with a simplified geometry, simulated MRI datasets (*BrainWeb* [18]), real T1-weighted MR images with typical resolution (1 mm^3 voxel), and high-resolution (sub-mm voxel size) images of explanted brains. The running time on

---

Algorithm 1 The level set function update algorithm.

{Compute time step for each point in the narrow band}
for all $\vec{r}_i \in NarrowBand$ **do**
{1. Compute the updated value}
$\phi_{new} \leftarrow \phi(\vec{r}_i, t_k) + \Delta t \Delta \phi(\vec{r}_i, t_k)$
{2. Check if there is a sign change}
if $sgn(\phi_{new}) == sgn(\phi(\vec{r}_i, t_k))$ **then**
{3.1 No sign change}
$\phi(\vec{r}_i, t_{k+1}) \leftarrow \phi_{new}$ {apply the update}
else if $\vec{r}_i \in S$ **then** {Check if is in the barrier}
{3.2 Is in the barrier, do not allow sign change}
$\phi(\vec{r}_i, t_{k+1}) \leftarrow \varepsilon$ {set to a small positive value}
else {3.3 Is clear; check for topology change}
  if $IsSimplePoint(\phi(\vec{r}, t_k), \phi_{new}, \vec{r}_i)$ **then**
  {3.3.1 No change in topology}
  $\phi(\vec{r}_i, t_{k+1}) \leftarrow \phi_{new}$ {apply the update}
  else {3.3.2 Do not allow topology change}
  $\phi(\vec{r}_i, t_{k+1}) \leftarrow \varepsilon \cdot sgn(\phi(\vec{r}_i, t_k))$ {set to a small value of the same sign}
  end if
end if
end for

---

a 2.6GHz AMD64 CPU with 4GB RAM was $\approx$ 10 min/1 hr for normal/high-resolution data respectively (similar to our implementation of ACE/TGDM). The algorithm runs significantly faster than the automatic topology fixer in FreeSurfer [2] (1-9 hr per hemisphere in normal-res.; N/A for high-res.). The following default parameters were used in all tests: (sect. II-A) maximal permittivity $\varepsilon_{\max} = 100$ (must be $\gg 1$, we tested 100 and 1000 with similar results), maximal potential $V_{max} = 100$ (arbitrary normalization); (sect. II-C) shock detection threshold $T = 0.8$ (determined empirically, similar to [5]), $d_{\min} = 1.5$ mm ($\sim$ minimum expected cortical thickness); (sect. II-D) probability threshold $P_0 = 0.6$ (can be tuned for a particular segmentation), sigmoid slope factor $K = 40$ (a steep sigmoid), curvature-term weight $w_\kappa = 0.1$ (may be increased for smoother surfaces), and 18-neighb. weights $w_i = 0.5/18$, $w_0 = 0.5$.

A. Simulated test cases

A simulated test image represents a spherical core ("WM", in darker gray) with two deep rectangular troughs ("sulcal folds"), overlayed by a layer of "GM" (in lighter gray) having unequal thickness at the opposing banks inside a trough; in one case (Fig. 1, left) GM banks are fully separated by background, and in another case (Fig. 2, left) the banks are fused at the periphery. Figures 1 and 2 show cross-sectional images of the Laplacian field (uniform permittivity $\varepsilon = 1$) in the middle, and images of our electric field model on the right. It can be seen that the ridge of the electric field (brighter pixels) is close to the "sulcal" center line, whereas the ridge of the Laplacian field is at the geometric center. Where the "sulcal" banks are fused, the ridge of the electric field follows a geometrically plausible path separating them (Fig. 2, right).
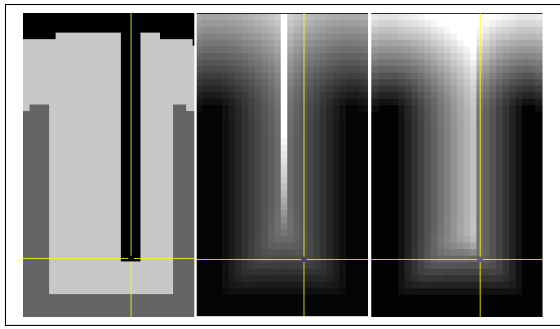
Fig. 1. Fragments of cross-sectional images of a test case representing a simulated sulcal fold (Left: two banks of unequal thickness, separated by background; Middle: the Laplacian field; Right: the electric field model).
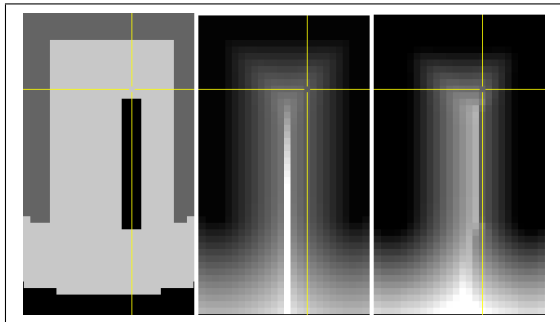

Fig. 2. Fragments of cross-sectional images of a test case representing a simulated sulcal fold (Left: two banks of unequal thickness, fused at the periphery; Middle: the Laplacian field; Right: the electric field model).

B. Simulated brain data

Simulated brain phantom MR images were generated for various image noise and intensity inhomogeneity conditions using the *BrainWeb* interface [18] (http://www.bic.mni.mcgill.ca/brainweb). Cortical reconstruction results showed good reproducibility across simulated noise and intensity artefacts conditions, as illustrated in Fig. 3. Figure 4 shows a zoomed in portion of an axial slice where the unresolved sulcal banks appear fused together, illustrating the separating skeleton and the resulting segmentation. In general, visual inspection demonstrated that the skeleton of the distance field is consistent with the skeleton generated by the ACE method, and in some areas has smoother properties.

C. Real MR images

Several T1-weighted MR images from a database of healthy adult subjects were used to test the algorithm performance on typical-resolution (1 mm^3 voxel) data (Fig. 5). In addition, the algorithm was evaluated on three high-resolution (0.25-0.35 mm^3 voxel size) images of explanted left brain hemispheres. Images in Fig. 6 show segmentation results for two different maximum distance constraint d_{max} values. The distance-constrained reconstruction allows extraction of "intermediate" surfaces at the specified maximum thickness level. This is illustrated in Fig. 7 by the example of the cortex in the central sulcus, where the primary
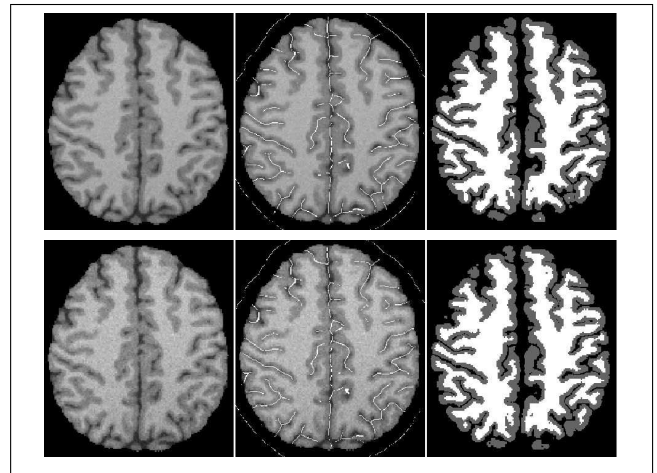

Fig. 3. Example axial slice of brain phantom images (Left column: source image; Middle column: overlayed with distance field skeleton; Right column: binarized cortical segmentation; Top row: noise 3%, inhomog. 20%; Bottom row: noise 5%, inhomog. 40%;).
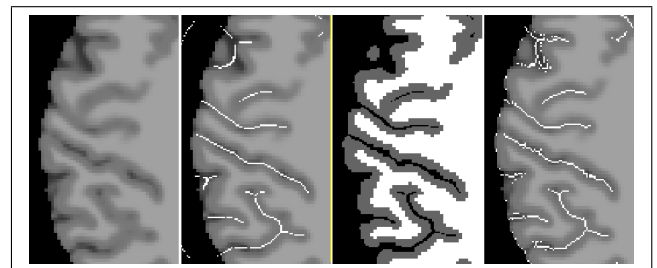

Fig. 4. Fragment of an axial slice of brain phantom images (Left to right: source image; overlayed with distance field skeleton; binarized cortical segmentation; overlayed with the ACE-generated skeleton).

motor cortex on the precentral bank is known to be thicker (mean 2.8 mm, sample range 2.5-3.5) than the primary somatosensory cortex on the postcentral bank (mean 1.9 mm, sample range 1.2-2.4) [19]. When the d_{max} parameter is gradually increased from 1.5 to 6 mm, distance-constrained reconstruction results show increasingly thicker bands in both banks, up to the point when the d_{max} reaches the local cortical thickness, in a manner consistent with the known neuroanatomy.

IV. CONCLUSION AND FUTURE WORK

We presented a novel PDE-based method for the reconstruction of the cerebral cortex from MR images. Although the algorithmic building blocks of our method were previously known to medical image processing community (*e.g.* [1], [9], [11]), the model of the potential field introduced here employs a novel combination of the algorithms, opening a different modelling perspective, and consolidating all algorithmic stages around one central aspect. The results show that the method is capable of reconstructing the outer cortical boundary with good geometric fidelity, while guaranteeing the preservation of the initial surface' topology. The algorithm is well suited for high-resolution images that can not be processed with the freely available software [2]. In addition,
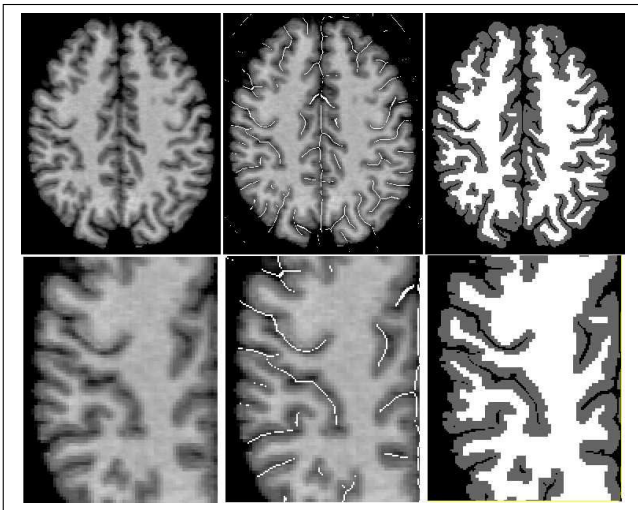
Fig. 5. Example of an axial slice of a real MR image (Left to right: source image; overlayed with distance field skeleton; binarized cortical segmentation).
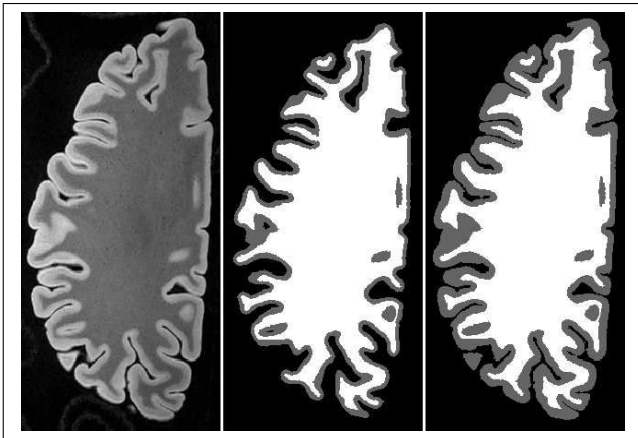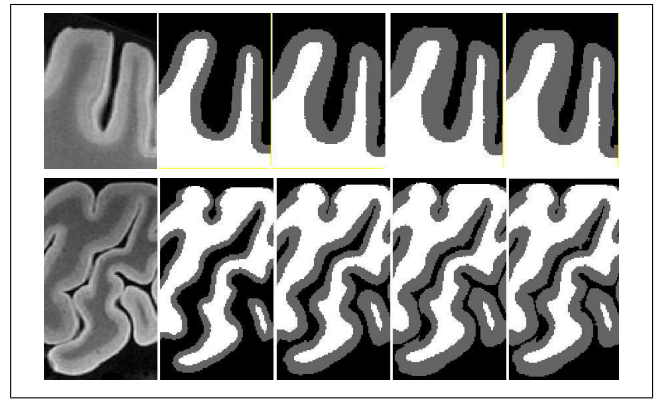

Fig. 7. Fragments of high-res. MR images featuring the central sulcus (Top row: sagittal slices; Bottom row: axial slices; Left to right: source image; binarized cortical segmentations with $d_{max} = 1.5$, 2.5, 3.5, and 6 mm). The primary motor cortex on the precentral bank (left bank on the images) is known to be thicker than the primary somatosensory cortex on the postcentral bank (right bank on the images), which is consistent with distance-constrained reconstruction results.

Fig. 6. Example of an axial slice of a high-resolution MR image (Left: source image; Middle and Right: binarized cortical segmentation with $d_{max} = 1.5$ mm and $d_{max} = 6$ mm, respectively).

it admits an optional constraint on cortical thickness, allowing generation of "intermediate" surfaces. Future work will address the accuracy and precision analysis of our method quantitatively, for example by cross-validation with other accepted cortical reconstruction methods like CRUISE [1], FreeSurfer [2], and CLASP [3].

REFERENCES

[1] X. Han, D. L. Pham, D. Tosun, M. E. Rettmann, C. Xu, and J. L. Prince. CRUISE: Cortical reconstruction using implicit surface evolution. *NeuroImage*, 23:997–1012, 2004.

[2] B. Fischl, A. Liu, and A. M. Dale. Automated manifold surgery: constructing geometrically accurate and topologically correct models of the human cerebral cortex. *IEEE Transactions on Medical Imaging*, 20(1):70–80, 2001.

[3] J. S. Kim, V. Singh, J. K. Lee, J. Lerch, Y. Ad-Dab'bagh, D. Mac-Donald, J. M. Lee, S. I. Kim, and A. C. Evans. Automated 3-D extraction and evaluation of the inner and outer cortical surfaces using a Laplacian map and partial volume effect classification. *NeuroImage*, 27(1):210–221, 2005.

[4] X. Zeng, L. H. Staib, R. T. Schultz, and J. S. Duncan. Segmentation and measurement of the cortex from 3-D MR images using coupled-surfaces propagation. *IEEE Transactions on Medical Imaging*, 18(10):927–937, 1999.

[5] X. Han, C. Xu, D. Tosun, and J. L. Prince. Cortical surface reconstruction using a topology preserving geometric deformable model. In *Proceedings of MMBIA*, pages 213–220, 2001.

[6] X. Han, C. Xu, and J. L. Prince. A topology preserving level set method for geometric deformable models. *IEEE Transactions on Pattern Analysis and Machine Intelligence*, 25(6):755–768, 2003.

[7] C. Xu and J. L. Prince. Snakes, shapes, and gradient vector flow. *IEEE Transactions on Image Processing*, 7(3):359–369, 1998.

[8] F. Kruggel, M. K. Brückner, T. Arendt, C. J. Wiggins, and D. Y von Cramon. Analyzing the neocortical fine-structure. *Medical Image Analysis*, 7(3):251–264, 2003.

[9] G. Gerig, O. Kubler, R. Kikinis, and F. A. Jolesz. Nonlinear anisotropic filtering of MRI data. *IEEE Transactions on Medical Imaging*, 11(2):221–232, 1992.

[10] W. H. Press, S. A. Teukolsky, W. T. Vetterling, and B. P.Flannery. Numerical Recipes in C++: The Art of Scientific Computing. Cambridge University Press, 2002.

[11] A. Yezzi and J. L. Prince. A PDE approach for measuring tissue thickness. In *Proceedings of CVPR*, pages I-87–I-92, 2001.

[12] K. Siddiqi, S. Bouix, A. Tannenbaum, and S. W. Zucker. The Hamilton-Jacobi Skeleton. In *Proceedings of ICCV*, pages 828–835, 1999.

[13] Y. Shi, P. M. Thompson, I. Dinov, and A. W. Toga. Hamilton-Jacobi Skeleton on Cortical Surfaces. *IEEE Transactions on Medical Imaging*, 27(5):664–673, 2008.

[14] S. Osher, and R. P. Fedkiw. Level set methods and dynamic implicit surfaces. New York: Springer, 2002.

[15] D. Adalsteinsson, and J. A. Sethian. A fast level set method for propagating interfaces. *Journal of Computational Physics*, 118(2):269–277, 1995.

[16] J. A. Sethian. A fast marching level set method for monotonically advancing fronts. *Proceedings of the National Academy of Sciences*, 93(4):1591–1595, 1996.

[17] G. Bertrand. A Boolean characterization of three-dimensional simple points. *Pattern Recognition Letters*, 17(2):115–124, 1996.

[18] D. L. Collins, A. P. Zijdenbos, V. Kollokian, J. G. Sled, N. J. Kabani, C. J. Holmes, and A. C. Evans. Design and construction of a realistic digital brain phantom. *IEEE Transactions on Medical Imaging*, 17(3):463–468, 1998.

[19] S. E. Jones, B. R. Buchbinder, I. Aharon. Three-dimensional mapping of cortical thickness using Laplace's Equation *Human Brain Mapping*, 11(1):12–32, 2000.